Systematic experimental investigation on the characteristics of molten copper fragmentation in water

Yangkai Huang[1], Shaojie Tan[1], Songbai Cheng[2, 1]*, Yinmeng Zhang[1], Hui Cheng[2, 1]

[1] Sino-French Institute of Nuclear Engineering and Technology, Sun Yat-Sen University, Zhuhai 519082, Guangdong, China

[2] College of Nuclear Science and Technology, Harbin Engineering University, Harbin 150001, Heilongjiang, China

*Corresponding author: chengsongbai@hrbeu.edu.cn (S. Cheng)

ABSTRACT

During severe accidents in light water reactors, thermal and hydraulic interactions play a crucial role in the Fuel-Coolant Interactions (FCI). Motivated to benefit the understanding on the fragmentation behavior of molten metallic fuel in water, in this study a series of simulated experiments is systematically conducted by injecting molten copper into a water pool. By adjusting parameters such as melt temperature, water temperature, melt penetration velocity, and water depth, the effects of these parameters on the fragmentation behavior of molten copper jet are investigated. It is found that water temperature determines the boiling mode during FCI, and at higher water temperatures, molten copper may not solidify and instead reach the bottom of the vessel in liquid form. When the melt temperature rises, the fragmentation process becomes less thorough, leading to an increase in the mass mean debris diameter. Higher penetration velocity of the molten metal results in smaller particles. A water depth greater than 70 cm has little effect on the fragmentation behavior. Weber number theory performs better in predicting the mass mean diameter of debris formed, comparing with the Rayleigh-Taylor and Kelvin-Helmholtz instability fragmentation theories.

Nomenclature

C_p Specific heat capacity (J/kg/K)

C_{pj} Specific heat capacity of the jet (J/kg/K)

C_{pw} Specific heat capacity of water (J/kg/K)

C Undetermined coefficient of the equation Weber number (-)

D Characteristic length of Reynold number (-)

d Diameter of the unstable droplet (mm)

d_m Mass mean diameter (mm)

d_v Volume mean diameter (mm)

g Gravitational acceleration (9.8m/s^2)

H_w Water depth (cm)

ΔP Pressure drop across the debris bed (Pa)

Re_w Reynolds number of water

T Temperature (°C)

T_{boil} Boiling temperature (°C)

T_m Melt temperature (°C)

$T_{m\text{-}p}$ Melting point (°C)

T_i Instantaneous interface temperature between the molten jet and water (°C)

T_{hn} Homogeneous nucleation temperature (°C)

T_{min} Minimum temperature difference for vapor film stability (°C)

T_h Hot liquid/molten material temperature (°C)

T_c Cold liquid/coolant temperature (°C)

T_w Water temperature (°C)

U_f Surface velocity of the fluid (m/s)

u Relative velocity between the two fluids at the interface (m/s)

V	Melt penetration velocity (m/s)
v	Volume of the fragment (ml)
$v_{particle}$	Volume of particles (ml)
v_{water}	Volume of water (ml)
We	Weber number (-)
x_k	Mass fraction of fragments in the ith size interval to the total mass (-)
ε	Porosity of the debris bed (-)
ρ_c	Density of the coolant (kg/m³)
ρ_f	Density of the fluid (kg/m³)
ρ_m	Density of the molten metal (kg/m³)
ρ_w	Density of water (kg/m³)
μ_f	Viscosity of the fluid (Pa·s)
$\lambda_{K\text{-}H}$	Critical wavelength of the Kelvin-Helmholtz instability (mm).
$\lambda_{R\text{-}T}$	Critical wavelength of the Rayleigh-Taylor instability (mm).
σ_m	Surface tension of the jet (N/m)
σ_c	Surface tension of the coolant (N/m)
φ	Sphericity of the debris bed (-)

1. Introduction

During a catastrophic core meltdown incident within a Pressurized Water Reactor (PWR), liquefied core material is anticipated to penetrate into coolant through high-velocity jet (Bürger et al., 1995; Cheng et al., 2021). In the pool, the fragmentation of the melt determines the further development of the accident. Inadequate fragmentation of the corium may compromise the structural integrity of the reactor pressure vessel's lower head, potentially leading to subsequent release of radioactive isotopes. Therefore, the fragmentation behavior of the molten jet plays a crucial role in the defense strategy in depth of nuclear safety. Due to the potential radiological threat and many uncertain negative impacts, Fuel-Coolant Interaction (FCI) has gained significant attention from researchers (Abe et al., 2006; Bürger et al., 1995; Cheng et al., 2020; Kondo et al., 1995).

A large number of experiments have been conducted to investigate the phenomena of FCI (Dinh et al., 1999; Iwasawa and Abe, 2018; Shen et al., 2018). These experiments can be categorized into oxide/water systems, metal/water systems, oxide/sodium systems, and metal/sodium systems. In addition to actual core materials such as UO_2, UO_2-ZrO_2, and uranium, various simulated melt materials have been used in FCI experiments, including Al_2O_3, Al_2O_3-FeO/Fe_2O_3, stainless steel, aluminum, copper, tin, zinc, Wood's metal, etc. (Gabor et al., 1988; Huhtiniemi et al., 1999; Magallon et al., 1999; Spencer et al., 1994)

Despite extensive research on the fragmentation behavior of molten jets, most studies have focused on the fragmentation of low-temperature molten materials in cooling water. There is still a lack of systematic experimental research on the fragmentation behavior of high-temperature molten materials in cooling water. Therefore, addressing the deficiencies in existing research, this paper conducts an experimental study on the fragmentation of molten copper jets in water. The physical properties of copper are

shown in Table 1. Both qualitative and quantitative methods are used to analyze the effects of melt temperature, water temperature, jet penetration velocity, and water depth on the fragmentation behavior of copper jets. The data obtained from the experiment can be used for the development and verification of severe accident analysis programs.

Table 1. Physical properties of copper

Properties	Copper[1]
Melting point (°C)	1083
Density (kg/m^3)	7998
Surface tension (mN/m)	1349
Kinetic viscosity (mm^2/s)	0.403
Latent heat of fusion (kJ/kg)	231
Heat capacity (J/kg·K)	543

Note:

1 - at 1083°C (Hu et al., 2019)

2 - at 2727°C (Hu et al., 2019; Leskovar and Uršič, 2009)

Preliminary studies have been conducted on the fragmentation behavior of copper (Hu et al., 2020; Yang et al., 2019). The multi-physics coupling mechanisms governing liquid-phase metallic copper/cryogenic fluid interactions are primarily manifested through synergistic thermal-hydraulic processes that enhance jet disintegration and oxide layer fracturing. This fragmentation behavior originates from: (1) phase-change-induced pressure fluctuations associated with vapor bubble dynamics; (2) multiphase interfacial instabilities amplified by thermal boundary layer interactions and momentum transfer; (3) viscous dissipation effects within the melt-coolant mixing zone, particularly intensified by rapid vaporization of entrained coolant droplets.

However, it should be noted that past researches on the thermal-hydraulic interactions between molten copper and coolant remain limited and primarily consist of qualitative studies with only a few instances, lacking a systematic investigation of the effects of various parameters.

In order to understand the influence of various parameters on the copper jet fragmentation behavior, a quantitative study was conducted on the characteristics of the debris bed. We designed an experimental setup using the high-frequency heating equipment at Sun Yat-sen University to melt copper and inject it into a water pool (Cheng et al., 2021). High-speed cameras were used to capture the fragmentation process, and fragment samples were collected. At the same time, measurement of the accumulated debris and fragments were conducted. Subsequently, we compared the fragmentation process and fragment samples under different parameters, and analyzed their effects on the fragmentation behavior of copper in water in combination with previous research findings. Finally, we use the criteria of Kelvin-Helmholtz instability, Rayleigh-Taylor instability, and Weber number theory to explain the fragmentation phenomenon of molten copper jet in coolant, and analyze the behavior modes of different situations (Iwasawa and Abe, 2019).

2. Experimental details

2.1 Experimental apparatus

Fig. 1 is the experimental apparatus for the fragmentation experiment of high-melting-point alloys. The experimental apparatus includes the following parts: stainless steel structural support, heating coil and crucible, ceramic plug with pulley assembly, a 47×47×150 cm rectangular water tank, a fragment collector, and a high-speed camera. Thermocouples are installed in both the crucible and water tank to track the thermal conditions of the molten material and coolant. The transparent vessel, constructed with heat-resistant glass, enables visual monitoring of the molten jet breakup process, with high-speed video recording capturing the fragmentation dynamics. The maximum temperature that can be measured by the thermocouples is 1300°C. The bottom of the crucible has an 8 mm diameter hole, which is sealed with a ceramic plug under natural conditions. The melting point of the alumina ceramic rod exceeds 2000°C, making it

reliable within the temperature range of the experiment. By pulling the steel wire, the ceramic plug can be lifted, allowing the molten copper to be injected into the water tank under the force of gravity.
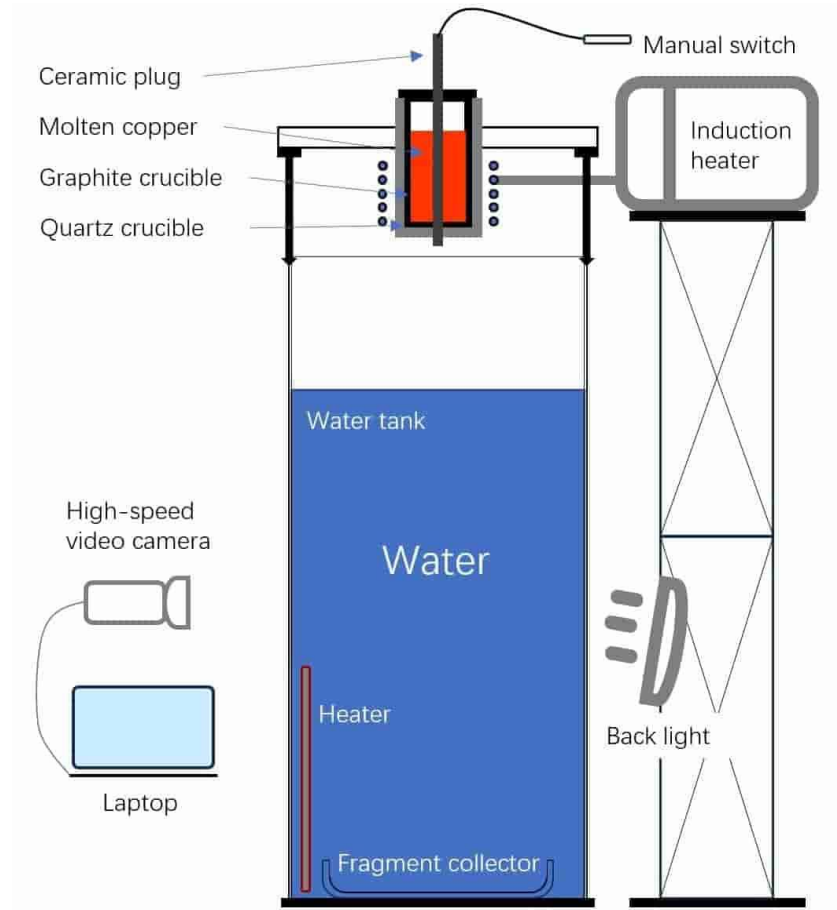

Fig. 1. The experimental apparatus

2.2 Experimental procedure and parameters

Before conducting each experiment, we carefully weighed and placed copper in the crucible. Then, we introduced the water into the glass water tank, keeping its depth at the required value. Several thermocouples were installed in relevant positions to measure the temperature of the heating copper and the water tank in real-time. If a higher water temperature is required, the water is heated to the predetermined temperature in advance. Then, we start the heating process of copper.

When the melt temperature reaches the predetermined value, the ceramic plug is pulled, and the melt falls into the water. At the same time, the acquisition button of the high-speed camera is pressed to capture the fragmentation behavior of the melt. After that, we collect samples for a series of measurements.

Table 2 shows the experimental parameters. In the table, the water depth (H_w) is the distance from the water surface to the collector. The melt penetration velocity (V) refers to the velocity of the melt when it reaches the water surface, which is calculated by

$$V = \sqrt{2gh} \tag{1}$$

where g refers to the acceleration of gravity and h refers to the distance from the crucible outlet to the water surface.

Table 2. Experimental conditions

Case No.	Copper mass (g)	Melt temperature (°C)	Water temperature (°C)	Water depth (cm)	Penetration velocity (m/s)
1	500	1100	25	60	3.13
2	500	1200	25	60	3.13
3	500	1300	25	60	3.13
4	500	1100	25	70	2.80
5	500	1200	25	70	2.80
6	500	1300	25	70	2.80
7	500	1100	25	130	3.13
8	500	1200	25	130	3.13
9	500	1300	25	130	3.13
10	500	1100	30	60	3.13
11	500	1100	40	60	3.13
12	500	1100	50	60	3.13
13	500	1100	60	60	3.13
14	500	1100	70	60	3.13
15	500	1200	25	110	3.13
16	500	1200	25	110	3.42
17	500	1200	25	110	3.70

Fig. 2 shows the schematic diagram of the possibility for the steam explosion. In the diagram, the vertical axis is the coolant temperature T_c and the horizontal axis is the molten material temperature T_h. A high possibility zone of the vapor explosion is so-

called Thermal Interaction Zone (TIZ). When the experimental conditions are closer to this region, there is a higher probability of the steam film collapsing and a steam explosion occurring. T_i represents the instantaneous interface temperature between the molten jet and water, T_{hn} is the homogeneous nucleation temperature, T_{min} is the minimum temperature difference for vapor film stability. At atmospheric pressure, the homogeneous nucleation temperature of water T_{hn} is approximately 314.1°C (Abe et al., 2004).

T_i is calculated by：

$$T_i = \frac{T_h - T_c}{1 + \sqrt{\beta}} + T_c \; , \beta = \frac{(\rho c_p k)_c}{(\rho c_p k)_h} \tag{2}$$

When $T_i = T_{min}$, the relationship between T_h and T_c is as follows:

$$T_i = T_{min} = T_h - T_{sat} = 101 + 4.1(T_{sat} - T_c)^{\frac{5}{4}} \tag{3}$$

where T_{sat} is saturation temperature of water. The boundaries of different regions can be obtained by using equations (2) and (3).
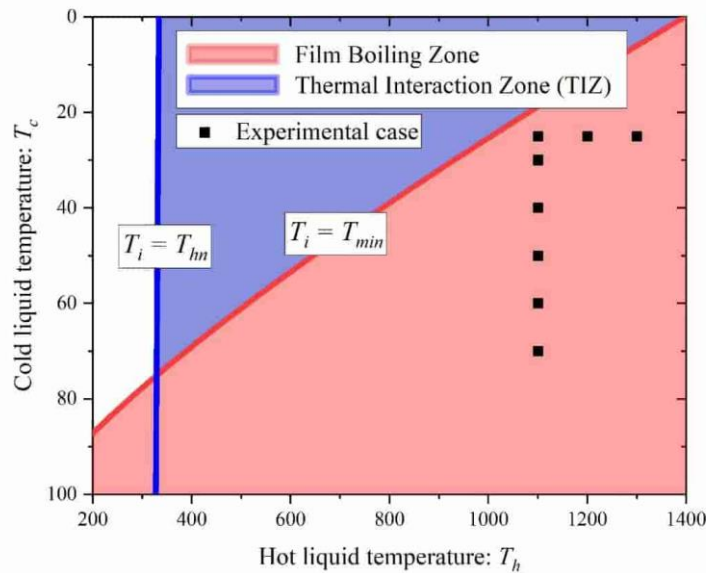

Fig. 2. Relationship between the molten jet and the coolant

2.3 Measurement quantities

Experimental analyses focused on quantifying key particulate metrics including average particle dimensions, size distribution patterns, as well as assessing porosity and sphericity within the aggregated fragments. By examining the characteristics of the debris bed, researchers can identify correlations between solidification processes and molten stream dynamics.

2.3.1 Size distribution of the fragments

After collecting the jet fragment samples and drying them, we used six sieves with sizes of 0.8mm, 1.5mm, 3.0mm, 6.0mm, 9.0mm, and 12.0mm, loading them into a vibrating machine for classification. Samples larger than 12.0mm were referred to as agglomerates, while the rest were classified as fragments. By measuring the mass distribution of the debris in each diameter interval, we were able to determine the thoroughness of the reaction. In this study, two mean diameters are calculated for subsequent analysis: the volume mean diameter (d_v) and the mass mean diameter (d_m).

The volume mean diameter is estimated as follows:

$$d_v = \frac{1}{\sum_{k=1}^{6} \frac{x_k}{d_i}} \tag{4}$$

where d_i denotes the mid diameter of the fragment in the ith size interval and x_k derived from the cumulative size distribution plot of the fragments. The mass mean diameter (d_m) is calculated as the fragment size that equally splits the total debris mass.

2.3.2 Debris bed porosity

The porosity (ε) of the debris bed is the ratio of void volume to the total bed volume, playing a key role in analyzing its cooling behavior. In this study, porosity was determined using the drainage method (Cheng et al., 2022, 2018) and calculated as:

$$\varepsilon = \frac{v_{total} - v_{particle}}{v_{total}} = \frac{v_{water}}{v_{total}} \tag{5}$$

where v_{total}, $v_{particle}$, and v_{water} denote the total debris bed volume, particle volume, and water volume, respectively.

2.3.3 Debris sphericity

In order to quantitatively estimate the morphology of the debris, its sphericity (φ) is defined as follows (Cheng et al., 2022, 2018):

$$\varphi = \frac{\pi^{\frac{1}{3}}(6v)^{\frac{2}{3}}}{A} \tag{6}$$

where A represents the surface area of the particles and v represents the volume of the particles. According to the Ergun equation (Ergun, 1952), the sphericity of fragments is calculated as follows:

$$\frac{\Delta P}{H_{pb}} = \frac{150(1-\varepsilon)^2 \mu_f U_f}{\varepsilon^3 (d_v \varphi)^2} + \frac{1.75(1-\varepsilon)\rho_f U_f{}^2}{\varepsilon^3 \varphi d_v} \tag{7}$$

Where the parameters are defined as: ΔP (pressure differential), H_{pb} (bed height), ε (void fraction), μ_f (fluid viscosity), U_f, (superficial velocity), d_v (volume-averaged particle diameter), φ (sphericity), and ρ_f (fluid density). The sphericity is determined through inverse modeling using the Ergun equation. A specialized test apparatus was developed to quantify fluid flow velocity and pressure gradient through particulate layers (Cheng et al., 2021).

3. Experimental results and discussion

In this section, we analyze and compare the data obtained from the experiments. We captured images of the molten metal jet injected into water at 0.05s, 0.3s, 0.6s, 0.9s, and 1.2s. Through these images, we can observe the evolution of the vapor interface during the fragmentation process of copper. Additionally, in experiments No. 1, 5, 6, 11, 12 and 15, we observed steam explosions. We captured instantaneous images of these explosions at a time interval of 0.0015s (1 frame).

3.1 Effect of melt temperature

Fig. 3, Fig. 4 and Fig. 5 depict the interaction process between molten copper jets and water, with jet temperatures of 1100℃, 1200℃, and 1300℃. From the figures, it can be observed that the size difference of the molten metal jets is not significant for different metal temperatures. When the jet break-up phenomenon occurs, numerous bubbles are generated along the sides of the jets (as shown in the red circles). From the images, it can be seen that the fragments assume a fixed shape after a certain distance, indicating that they have cooled and primarily fall in a solid state (as shown in the blue circles). Black smoke was observed in some cases, which was composed of copper powder caused by steam explosions.

| 0.05s, | 0.3s, | 0.6s, | 0.9s, | 1.2s |

(a) $T_m = 1100°C$

| 0.05s, | 0.3s, | 0.6s, | 0.9s, | 1.2s |

(b) $T_m = 1200°C$

| 0.05s, | 0.3s, | 0.6s, | 0.9s, | 1.2s |

(c) $T_m = 1300°C$
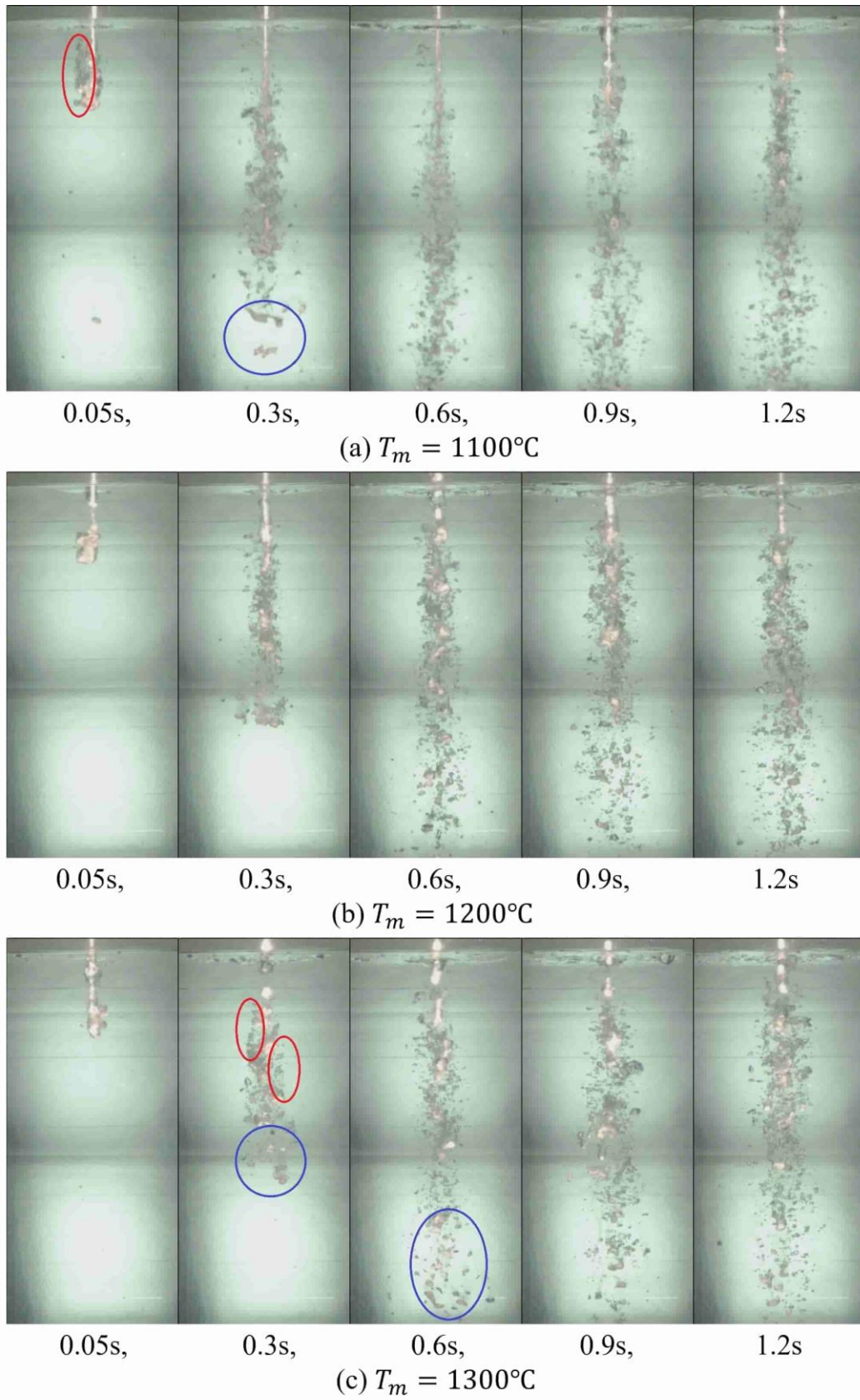
Fig. 3. Visual results of fragmentation process at different melt temperatures
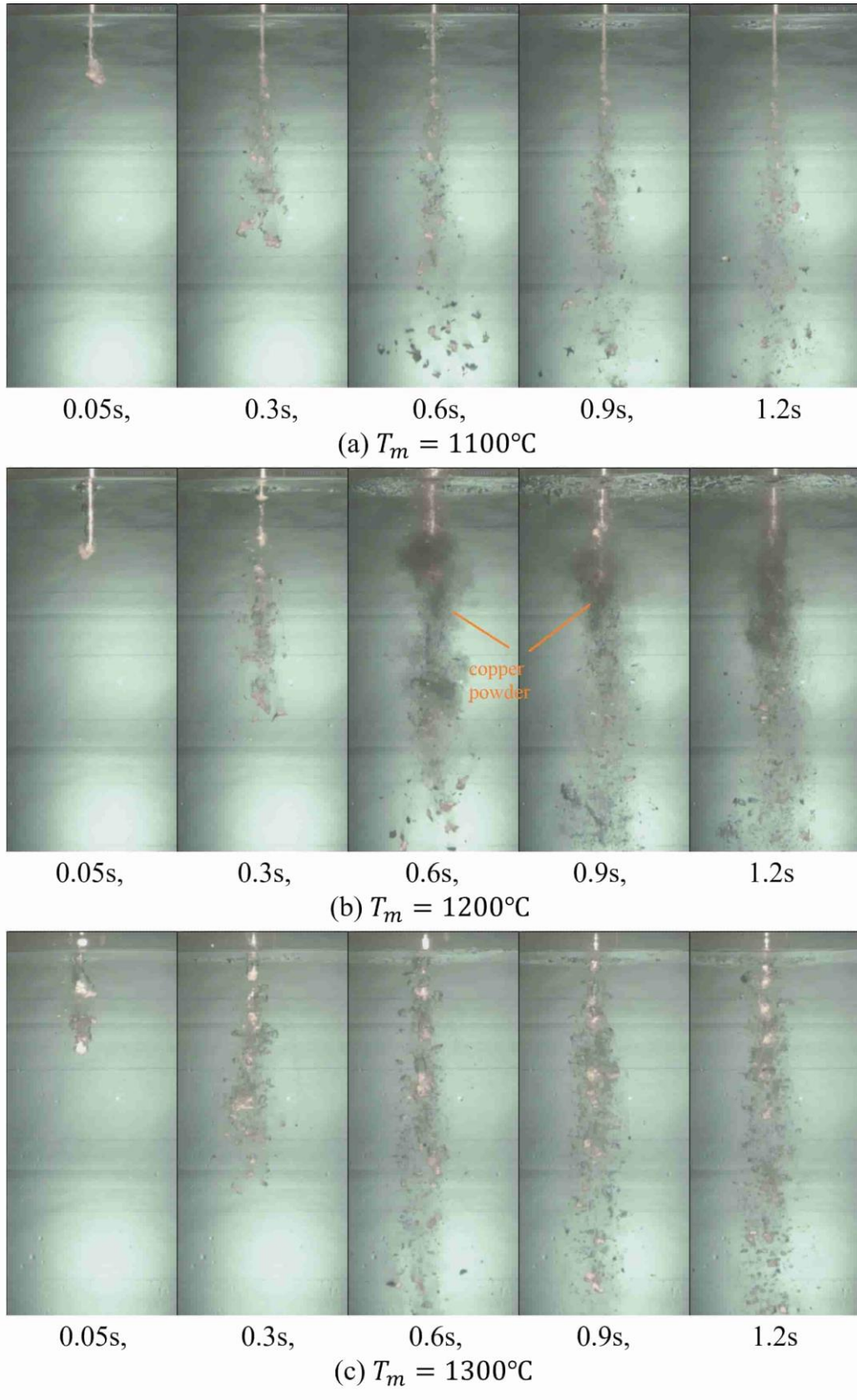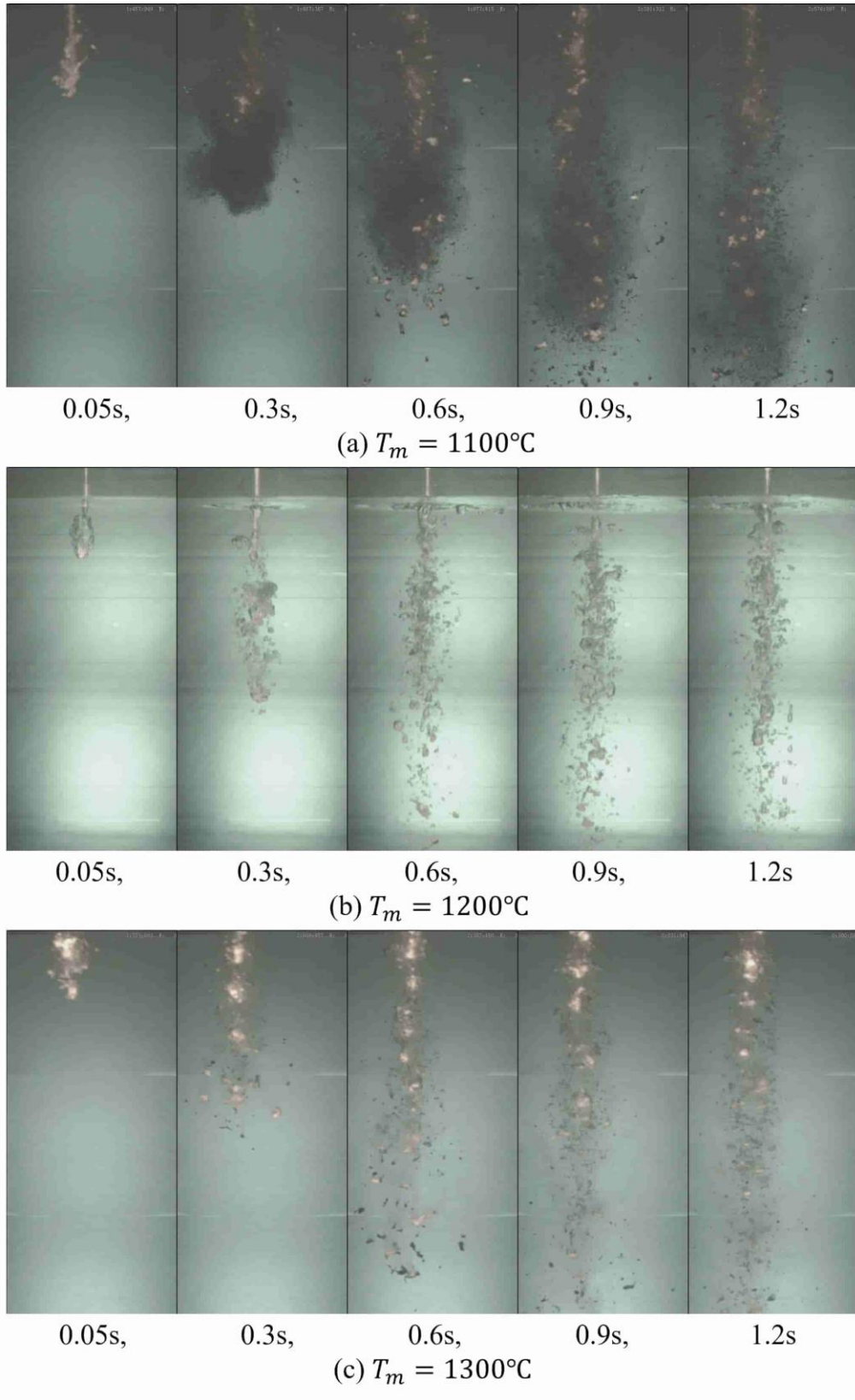
$(T_w = 25°C, H_w = 60cm, V = 3.13m/s)$

1

| 0.05s, | 0.3s, | 0.6s, | 0.9s, | 1.2s |

(a) $T_m = 1100°C$

| 0.05s, | 0.3s, | 0.6s, | 0.9s, | 1.2s |

copper
powder

(b) $T_m = 1200°C$

| 0.05s, | 0.3s, | 0.6s, | 0.9s, | 1.2s |

(c) $T_m = 1300°C$

Fig. 4. Visual results of fragmentation process at different melt temperatures

$(T_w = 25°C, H_w = 70cm, V = 2.8m/s)$

1

0.05s,   0.3s,   0.6s,   0.9s,   1.2s

(a) $T_m = 1100°C$

0.05s,   0.3s,   0.6s,   0.9s,   1.2s

(b) $T_m = 1200°C$

0.05s,   0.3s,   0.6s,   0.9s,   1.2s

(c) $T_m = 1300°C$

Fig. 5. Visual results of fragmentation process at different melt temperatures

$(T_w = 25°C, H_w = 130cm, V = 3.13m/s)$

1

Fig. 6, Fig. 7 and Fig. 8 show the debris bed at jet temperatures of 1100℃, 1200℃, and 1300℃. From the figure, it can be observed that due to incomplete cooling of the fragments, agglomerates have formed when the water depth is within 70cm. Besides, it can be seen that fragments are larger with the increase of melt temperature.

(a) $T_m = 1100℃$
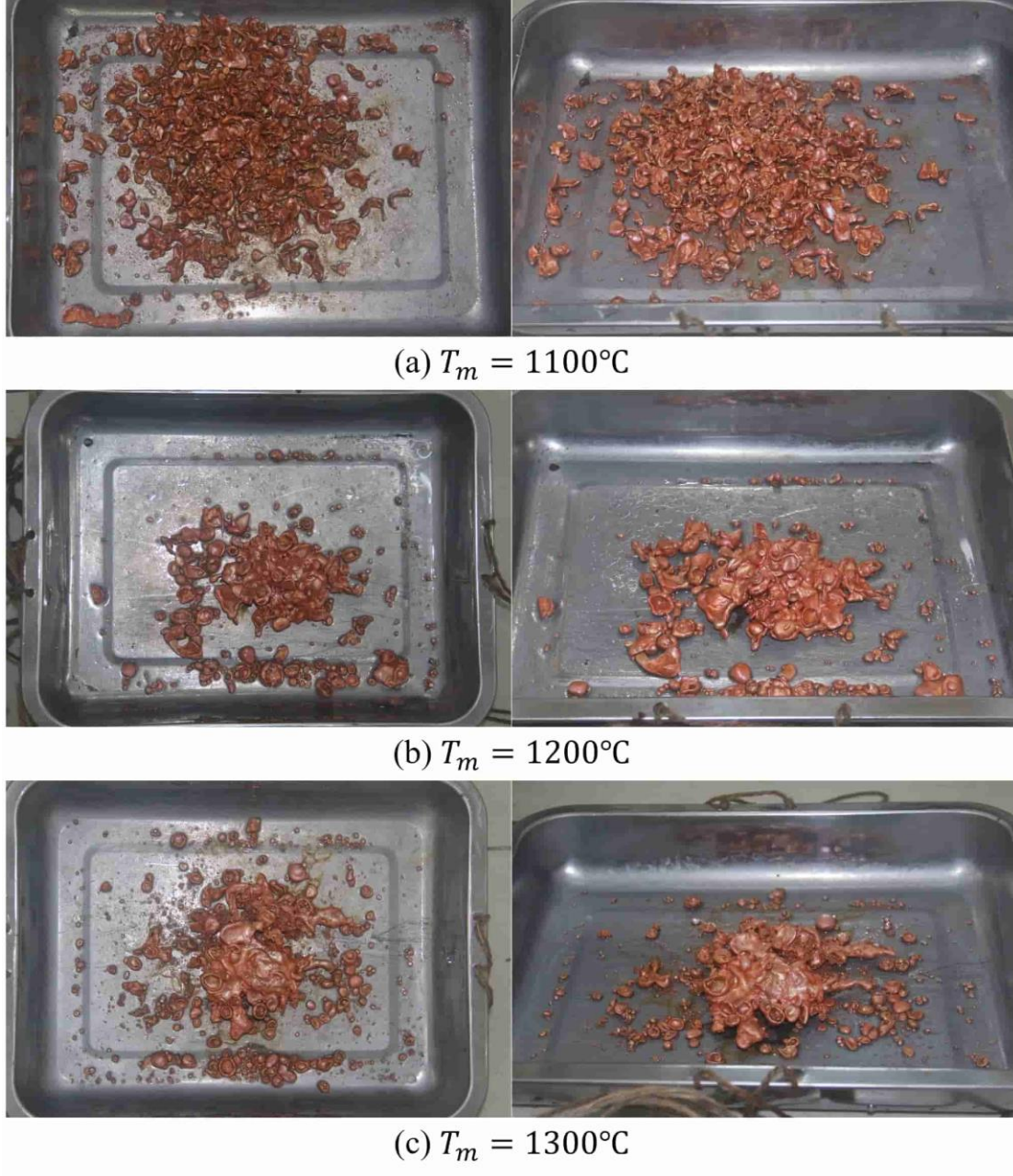
(b) $T_m = 1200℃$

(c) $T_m = 1300℃$

Fig. 6. Photographs of the debris bed at different melt temperatures

$(T_w = 25\ ℃, H_w = 60cm, V = 3.13m/s)$

(a) $T_m = 1100°C$

(b) $T_m = 1200°C$

(c) $T_m = 1300°C$

Fig. 7. Photographs of the debris bed at different melt temperatures

$(T_w = 25°C, H_w = 70cm, V = 2.8m/s)$
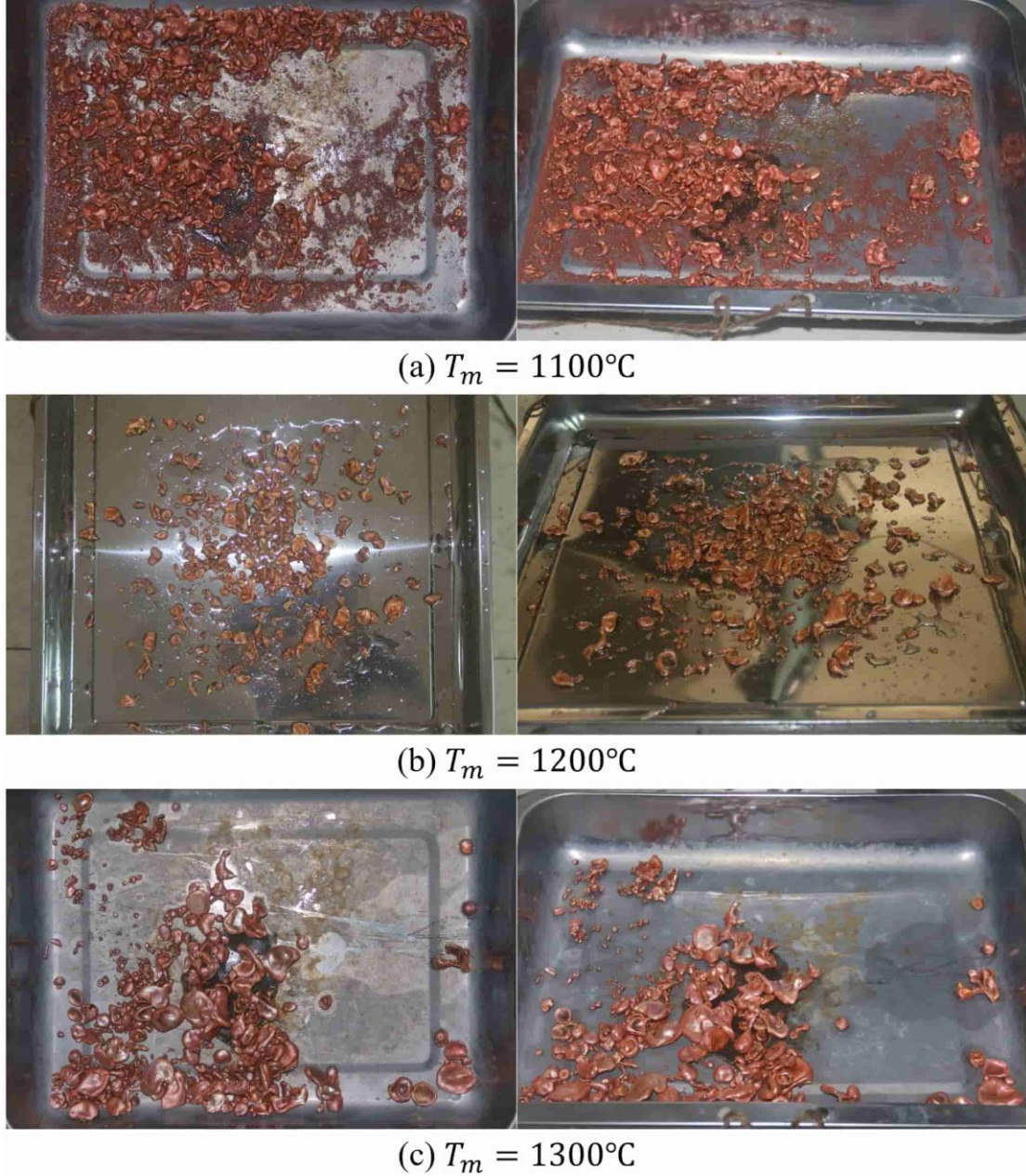
Fig. 8. Photographs of the debris bed at different melt temperatures

$(T_w = 25°C, H_w = 130cm, V = 3.13m/s)$

Fig. 9 shows the physical properties of the debris bed. In this experiment, when the water depth is not larger than 70cm, and the jet temperature is set to 1300°C, most fragments have not completely solidified when reaching the bottom of the water tank. As they weld together and form large agglomerates, it is hard to measure their size distribution.

Fig. 9 (a)-(c) demonstrate that the debris bed exhibits a predominant particle size distribution peak within the 6-9 mm range. As the jet temperature increases, the proportion of fragments with diameters in the range of 9-12mm increases. Notably, a 100°C temperature increment in molten material (from 1100°C to 1200°C) induces significant redistribution, manifesting as reduced prevalence of 6-9 mm particulates. This results in an increase in the mass mean diameter of the fragments, shown in Fig. 9 (d). The curves for 1200°C and 1300°C are relatively close, possibly due to a marginal effect.

It can be concluded that higher jet temperatures lead to less complete fragmentation, which presents a conclusion opposite to that of low-melting-point alloys. In previous studies on the fragmentation of lead-bismuth eutectic (LBE) (Cheng et al., 2021), as the temperature of the melt increases, the mass mean diameter of the fragments decreases. This is because the LBE jet is sufficiently fragmented and cooled in a short time after entering the coolant, with higher melt temperatures delaying the solidification of LBE in water, leading to more thorough fragmentation. However, for high-melting-point metals like copper, after the jet is fragmented, many fragments cannot be sufficiently cooled and may even remain in a liquid state. The stable film boiling during the debris descent prevents some fragments from completely solidifying, causing them to merge and form larger fragments. As the temperature of the melt increases, the fragments become more difficult to solidify, leading to an increase of larger debris. Additionally, we observed steam explosions in some groups, which produced a significant amount of metal powder.

As indicated in Fig. 9 (e) and (f), raising the melt temperature has the effect of rendering the debris bed more compact, with an increase of debris sphericity. As the heat transfer between the molten copper droplets and water occurs within the range of film boiling, the vapor film surrounding the molten copper droplets remains stable, resulting in a slower heat transfer rate as these vapor films and steam bubbles provide a certain isolation effect on the molten copper. This makes the surface of the solidified copper
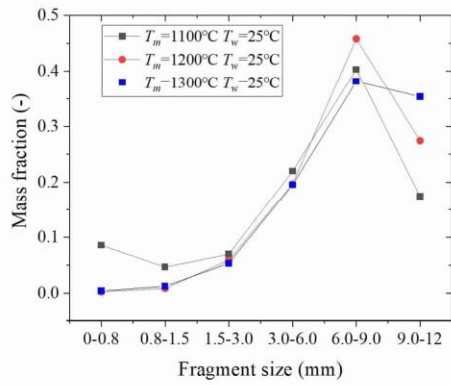
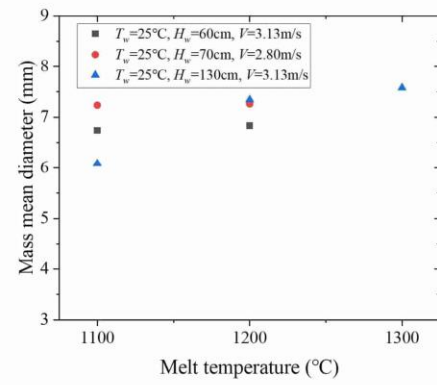smoother due to the effect of surface tension, and the fragments tend to be closer to a spherical shape.
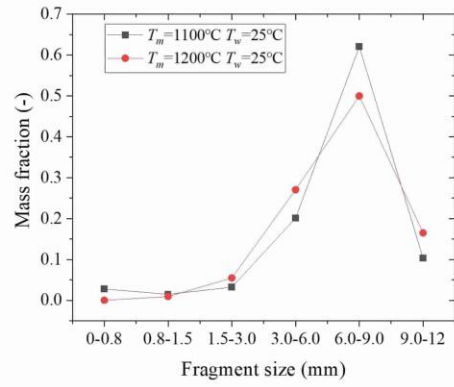
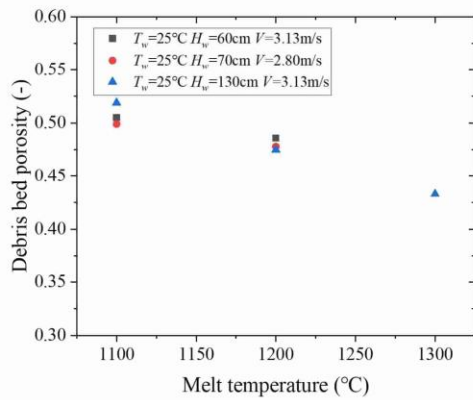(a) Fragment size distribution
$(T_w = 25°C, H_w = 60cm, V = 3.13m/s)$
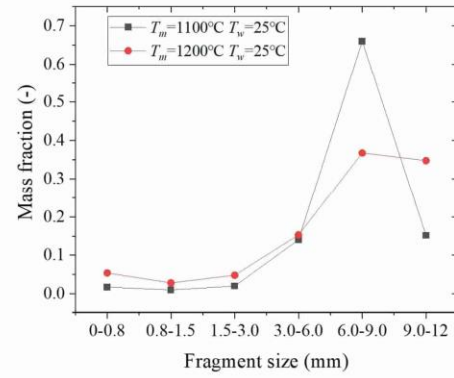
(b) Fragment size distribution
$(T_w = 25°C, H_w = 70cm, V = 2.8m/s)$

(c) Fragment size distribution
$(T_w = 25°C, H_w = 130cm, V = 3.13m/s)$

(d) Mass mean diameters

(e) Debris bed porosity
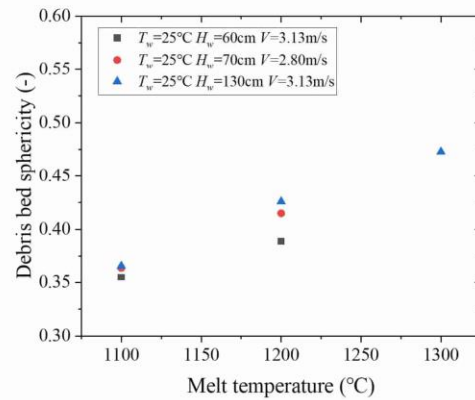
(f) Debris sphericity

Fig. 9. Physical properties of the debris bed at different melt temperatures

3.2 Effect of water temperature

Fig. 10 shows the interaction process between a copper molten jet and water under the following parameters: jet temperature of 1100℃, jet velocity of 3.13m/s, water depth of 60cm, and water temperatures of 25℃, 30℃, 40℃, 50℃, 60℃ and 70℃. From the images, it can be observed that the jet undergoes fragmentation and generates a large number of bubbles after entering the water. At lower water temperatures (25℃ and 30℃), the steam bubbles are smaller and more densely distributed. The droplets separated from the molten metal jet no longer change shape (as shown in the blue circles) and produce few steam bubbles in their surroundings, indicating that they have solidified. At higher water temperatures (higher than 30℃), we can observe that the splintered droplets are encapsulated within a vapor film (as shown in the red circles) and still undergoing deformation during their descent, indicating that they have not yet solidified. These metal droplets maintain their liquid state and continue to generate a large number of bubbles until they reach the bottom of the water tank, where they accumulate and form large agglomerates.
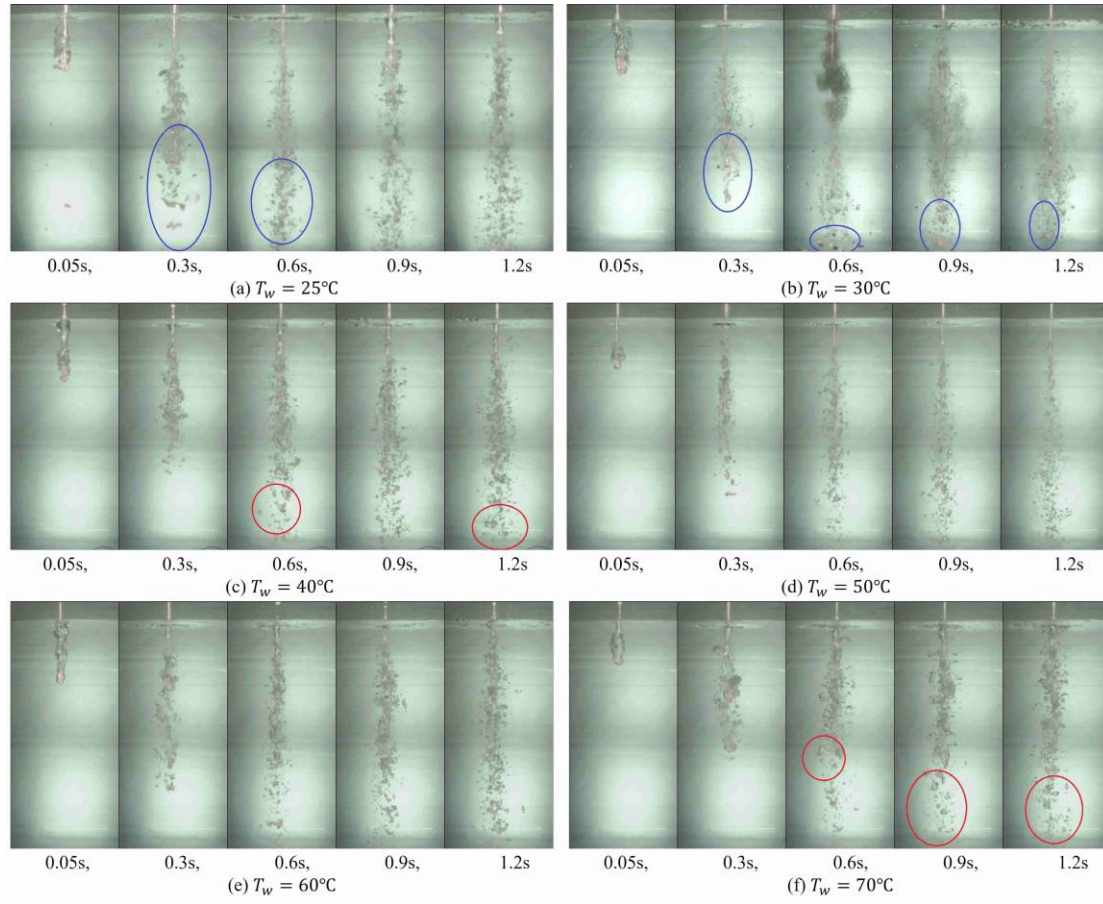
Fig. 10. Visual results of fragmentation process at different water temperatures

$$(T_m = 1100°C, H_w = 60cm, V = 3.13m/s)$$

Fig. 11 shows the debris bed observed in the experiments. The vapor film surrounding the molten metal droplets ruptures during the descent, and the molten metal cools and eventually accumulates at the bottom in the form of fragments. From Fig. 10, it can be observed that these jets have undergone fragmentation when the water temperature is higher than 30°C. However, in the catcher, these fragments are consolidated into an agglomerate, as shown in Fig. 11. This indicates that the jets remain above the copper's melting point throughout the contact with water, preventing solidification during descent. The metal jets and the splintered droplets fall to the bottom of the water tank and coalesce in a liquid state.

Based on the above, it can be concluded that higher water temperatures increase the mass fraction of the aggregates and inhibit the fragmentation phenomenon. After the jet

contacts the water, rapid heating and vaporization of the water occur, and the higher the water temperature, the more intense the evaporation, leading to the formation of thicker and more stable vapor films. Subsequently, due to certain fluid dynamic factors (such as Rayleigh-Taylor instability), the vapor films rupture, resulting in fragmentation of the jet front and the generation of a large number of bubbles. Meanwhile, the vapor film on the interface between the molten material and the coolant rapidly condenses, transitioning the main heat transfer mechanism from film boiling to nucleate boiling, with a possibility of steam explosion. Although the overheated copper surface comes into contact with the coolant, the coolant cannot penetrate the interior of the molten copper but rapidly evaporates on the overheated surface. Therefore, the surface of the fragments remains relatively smooth and intact, resulting in a higher sphericity of the copper fragments (as shown in the red circles).

When the water temperature rises to 40°C, the fragmented jets re-solidifying at the bottom. High water temperature kept this set of experiments away from the Thermal Interaction Zone, as shown in Fig. 2. The vapor films can maintain around the jet for longer time in this case, significantly impeding heat exchange between the jet and water and preventing solidification from occurring effectively.
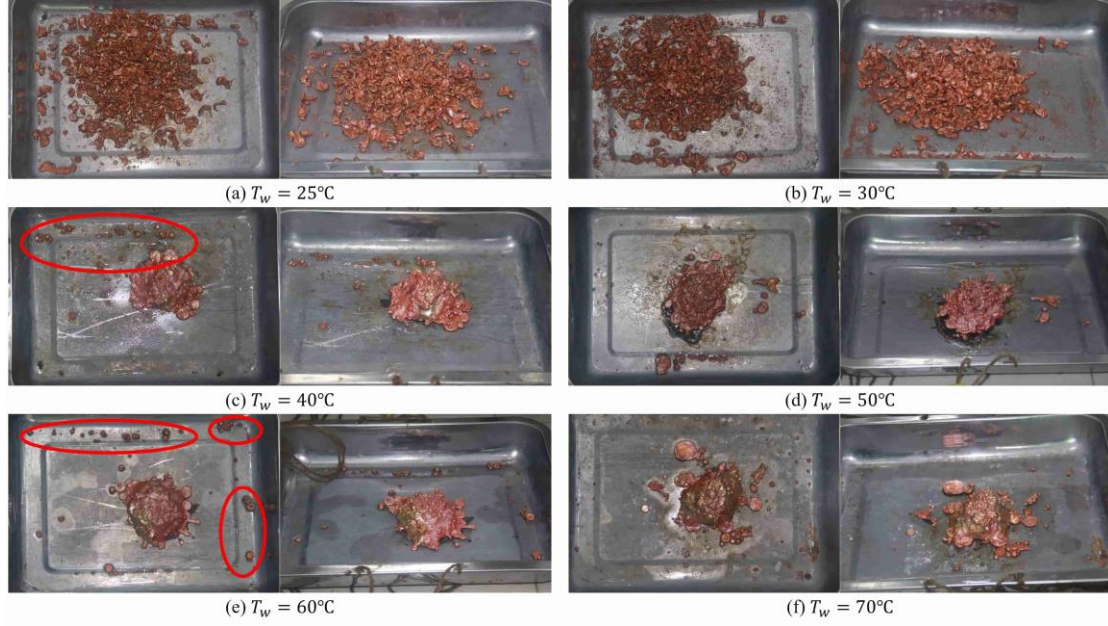
Fig. 11. Photographs of the debris bed at different water temperatures

$(T_m = 1100℃, H_w = 60\text{cm}, V = 3.13\text{m/s})$

In previous studies on LBE alloys, the transformation of this debris bed morphology occurred at a water temperature of 90℃ (Cheng et al., 2021). This is mainly because the melting temperature of copper (1083℃), being much higher than that of LBE alloy (125℃), maintains film boiling on the copper-water surface for a prolonged period. Besides, the high thermal conductivity of copper results in a smaller temperature gradient on the surface of copper debris, leading to a more stable interface.

3.3 Effect of melt penetration velocity

In this section, the jet temperature is set to 1200℃, while the water temperature is 25℃ and the water depth is 110cm. As per the research by Dinh et al. in 1999 (Dinh et al., 1999), from a hydrodynamic perspective, the relative velocity between two fluids has a significant impact on the fragmentation process.

Fig. 12 shows the interaction at jet velocities of 3.13m/s, 3.42m/s, and 3.70m/s. From the images, it can be observed that fragmentation occurs within the first 15cm after the

jet enters the water. The fragmentation process shows no significant variation across different penetration velocities. Similarly, the number and size of bubbles produced during this process also remain largely the same.
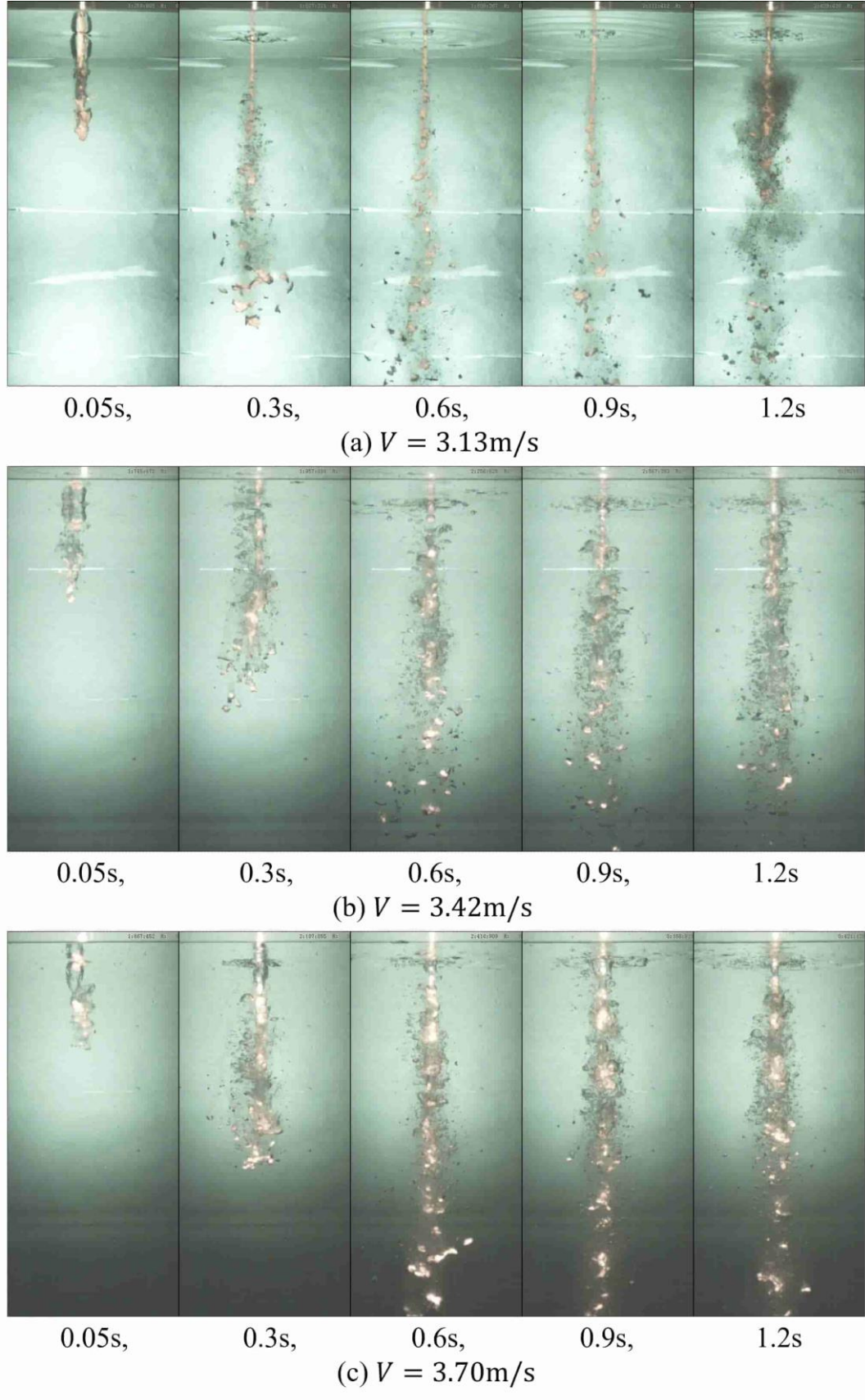
| 0.05s, | 0.3s, | 0.6s, | 0.9s, | 1.2s |

(a) $V = 3.13$m/s

| 0.05s, | 0.3s, | 0.6s, | 0.9s, | 1.2s |

(b) $V = 3.42$m/s

| 0.05s, | 0.3s, | 0.6s, | 0.9s, | 1.2s |

(c) $V = 3.70$m/s

Fig. 12. Visual results of fragmentation process at different melt penetration velocity and water depth

$(T_m = 1200℃, T_w = 25℃, H_w = 110cm)$

2

Fig. 13 shows some fragments samples we obtained, demonstrating the debris bed formed by the collector at the bottom of the water tank for the corresponding group experiment in Fig. 12. We can observe that there is no significant difference among the morphologies of the debris bed with different penetration velocities.

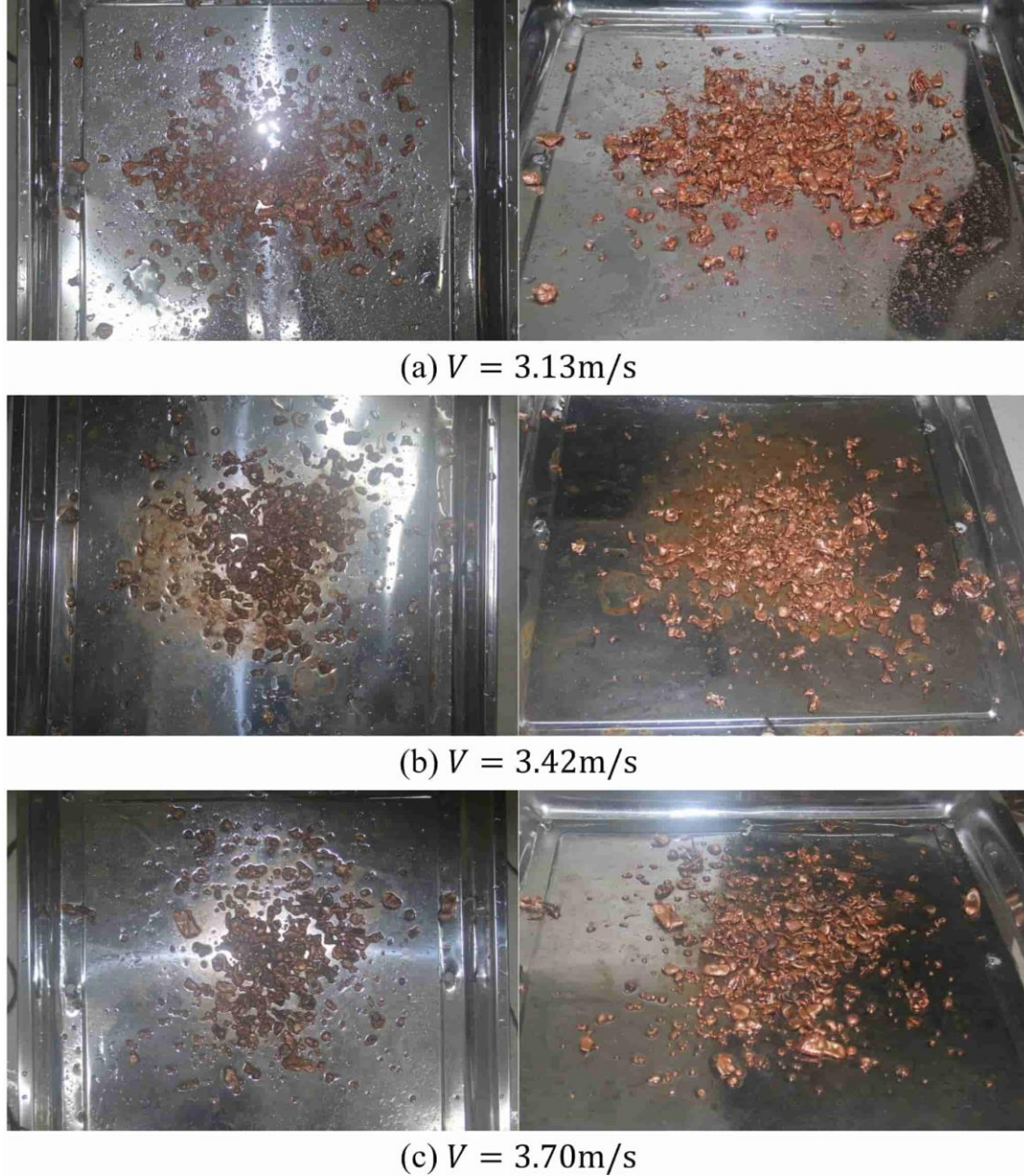Fig. 13. Photographs of the debris bed at different penetration velocity

$(T_m = 1200°C, T_w = 25°C, H_w = 110cm)$

错误!未找到引用源。Fig. 14 illustrates the physical properties of the debris bed. It can be observed that the higher the penetration velocity of the molten copper jet, the

stronger the fragmentation effect became, resulting in smaller fragmented products. This is consistent with the conclusions of previous experiments on LBE (Cheng et al., 2021).

Considering the deviation, the penetration velocity exerts no significant impact on the debris bed's porosity and the fragmented particles' sphericity, as shown in Fig. 14 (c) and (d). Based on previous studies (Cheng et al., 2021), the sphericity of the fragments is greatly influenced by thermal factors. Under the conditions where the stacking method and the shape of the fragments are similar, when the jet's penetration velocity is higher, the diameter of the fragmented particles decreases approximately proportionally, and the morphology of the debris bed does not change significantly.
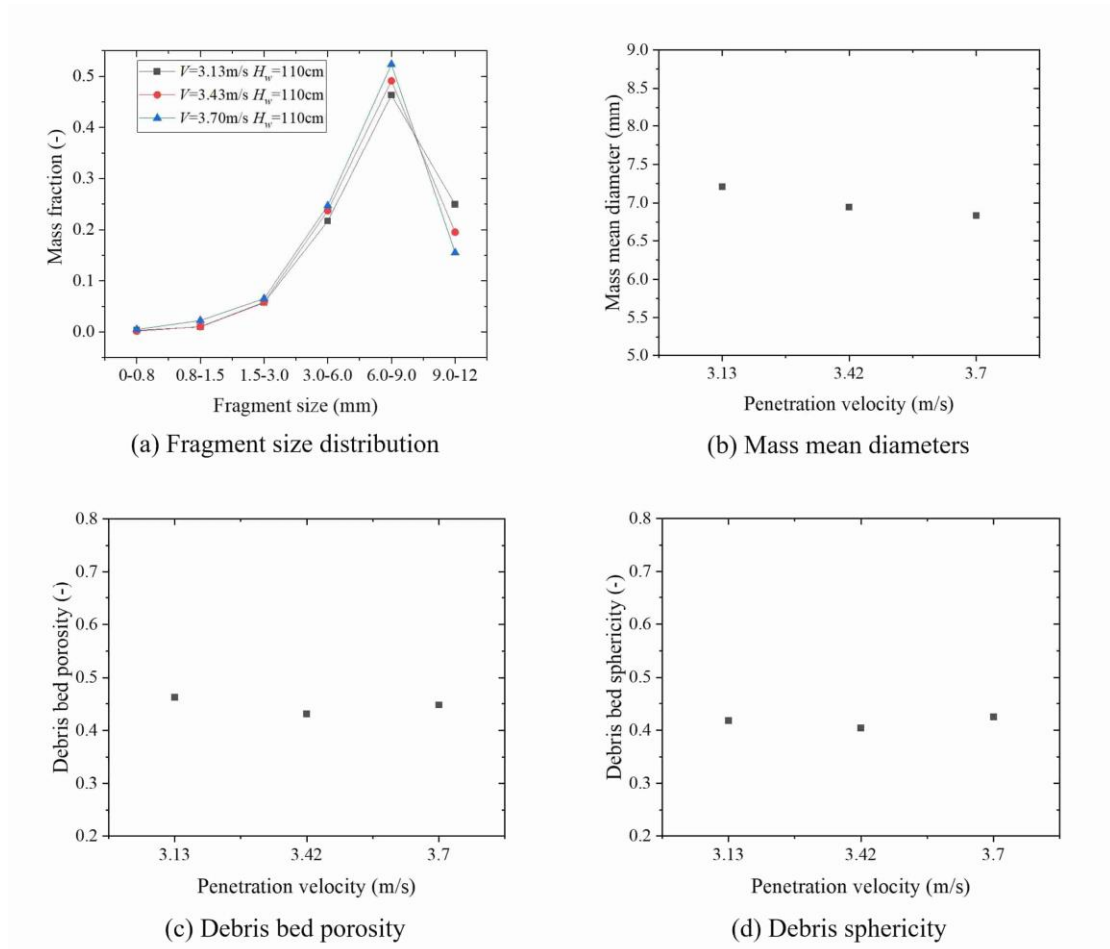

(a) Fragment size distribution

(b) Mass mean diameters

(c) Debris bed porosity

(d) Debris sphericity

Fig. 14. Physical properties of the debris bed at different penetration velocity

$(T_m = 1200°C, T_w = 25°C, H_w = 110cm)$

3.4 Effect of water depth

In this section, the jet temperature is set to 1200°C, while the water temperature is 25°C and the penetration velocity is 3.13m/s.

Fig. 15 shows the interaction process between the molten copper jet and water at water depth of 60cm, 110cm, and 130cm. From the images, it can be observed that there is no significant difference in the fragmentation process among different water depth, and the number and size of bubbles generated during the fragmentation process are also not significantly different. When the water depth was 110cm, a steam explosion occurred.

0.05s,   0.3s,   0.6s,   0.9s,   1.2s

(a) $H_w = 60$cm

0.05s,   0.3s,   0.6s,   0.9s,   1.2s

(b) $H_w = 110$cm

0.05s,   0.3s,   0.6s,   0.9s,   1.2s

(c) $H_w = 130$cm
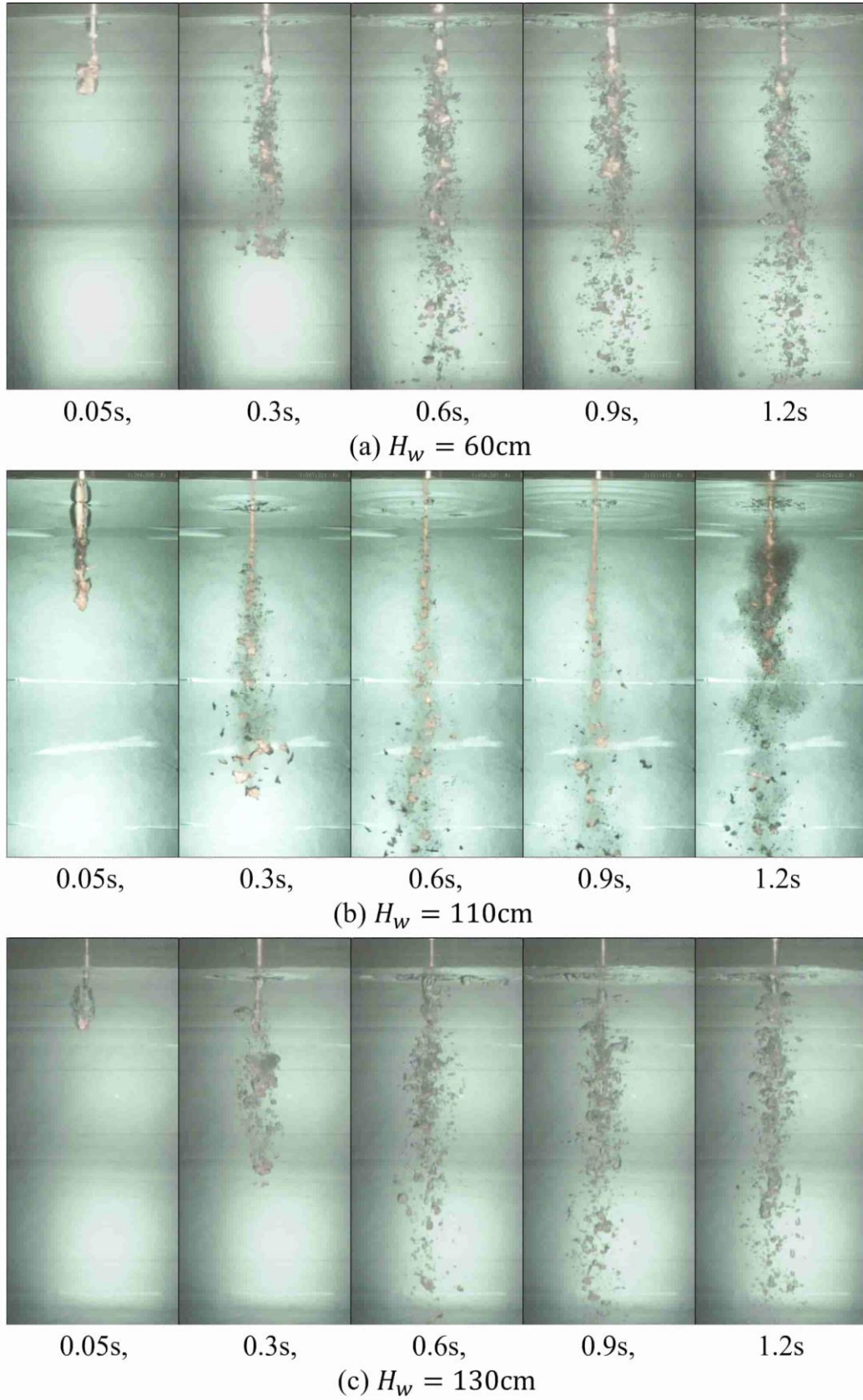
Fig. 15. Visual results of fragmentation process at different water depth

$(T_m = 1200℃, T_w = 25℃, V = 3.13\text{m/s})$

Fig. 16 presents the debris bed's morphology at different water depths. It can be clearly seen that the debris bed's morphology at a 60cm water depth is markedly distinct from that at 110cm and 130cm. At a water depth of 60cm, the fragments did not cool sufficiently, resulting in the formation of large agglomerates at the bottom. The morphologies of the debris beds at water depths of 110cm and 130cm are similar.
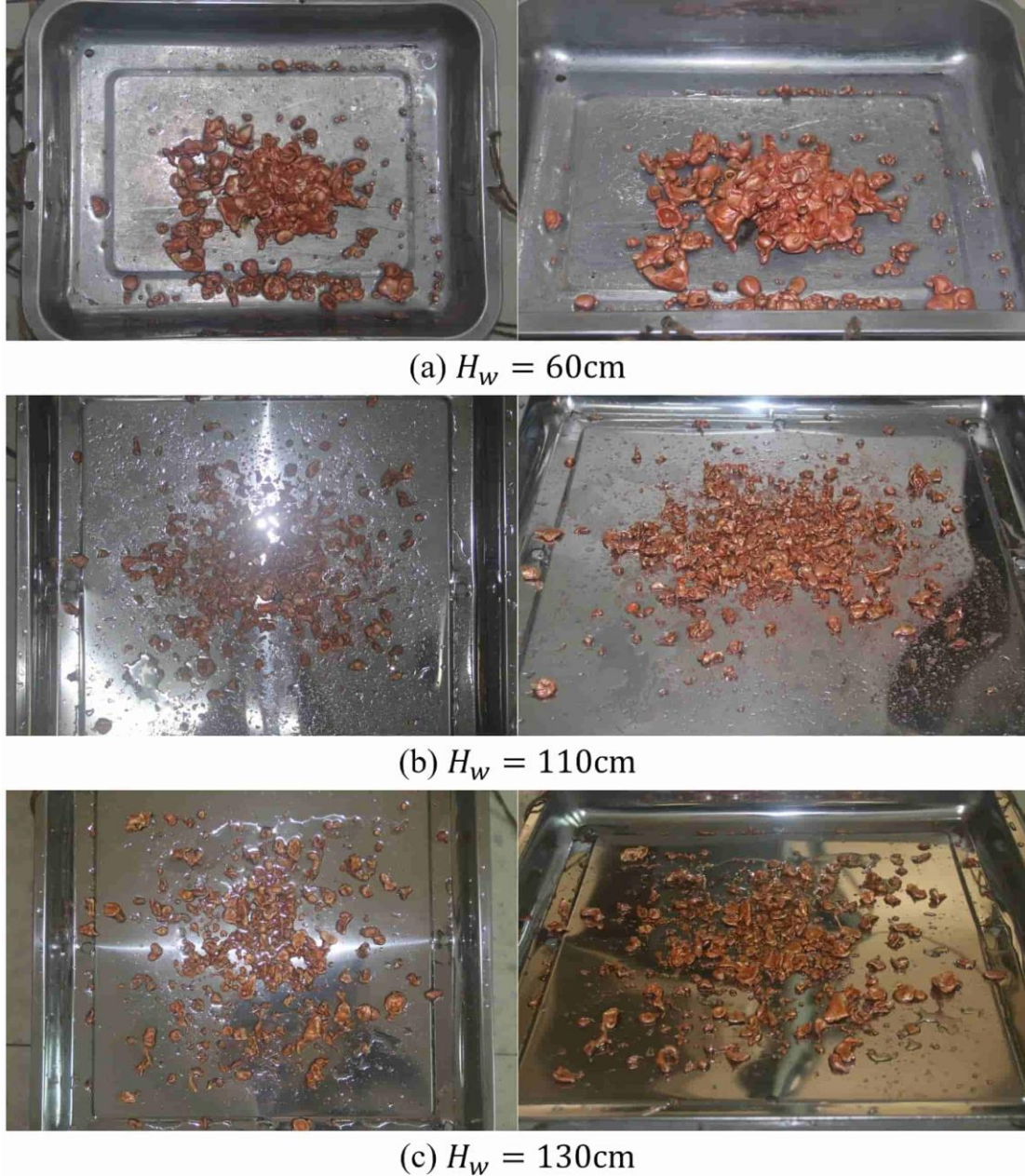

(a) $H_w = 60$cm

(b) $H_w = 110$cm

(c) $H_w = 130$cm

Fig. 16. Photographs of the debris bed at different water depth

$(T_m = 1200°C, T_w = 25°C, V = 3.13\text{m/s})$

Fig. 17 illustrates the physical properties of the debris bed. It can be observed that as the water depth increases, the proportion of debris with diameters of 3-9 mm decreases, while the count of debris with diameters of 9-12 mm increases. This may be because during the falling process, the jet, after being fragmented, has not yet solidified, and some small fragments fuse to form larger ones.

As shown in Fig. 17 (c) and (d), the water depth exerts minimal impact on the debris bed's porosity. Nevertheless, the sphericity of the fragmented particles demonstrates a slight increasing trend when the water is deeper. This might be because in the case of relatively shallow water, the fragments cannot completely cool down. When these uncooled molten coppers reach the fragmentation product collector, they alter the original shape, reducing the sphericity of the fragmented particles. However, there is no significant change in the way that the debris bed forms, so the porosity of the debris bed does not change significantly.
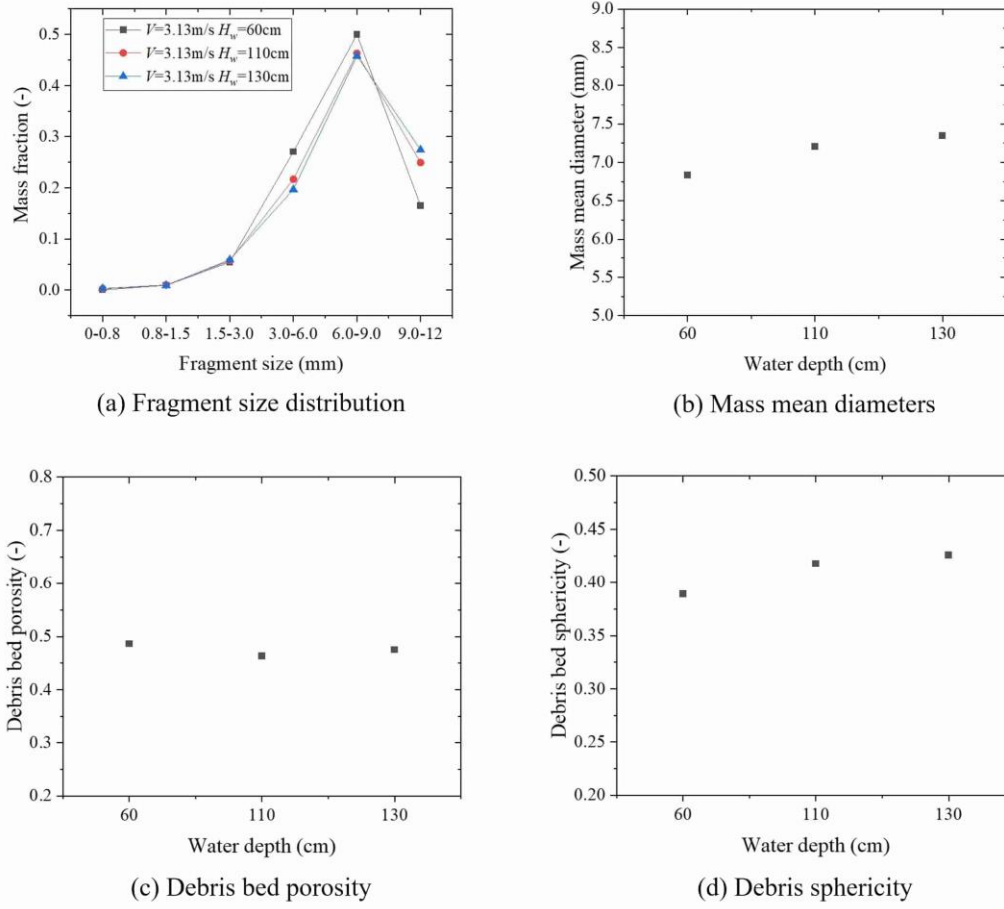
Fig. 17. Physical properties of the debris bed at different water depth

$(T_m = 1200°C, T_w = 25°C, V = 3.13\text{m/s})$

3.5 Discussion on triggering factors of steam explosion

Fig. 18 shows the specific process of steam explosions with a screenshot interval of approximate 0.0015 seconds (1 frame) in experiments No. 1, 5, 6, 11, 12 and 15. It can be observed that steam explosions typically start with a fragment, followed by the propagation of shock waves to surrounding fragments, causing them to explode as well, resulting in a chain reaction. These explosions lead to the presence of a large amount of metal dust in the water tank.

In Section 3.2, which explores the effect of water temperature on the behavior of molten jet fragmentation, the jet temperature was controlled at 1100°C. When the water

temperature was set at 25°C and 30°C, steam explosions were observed. However, at higher water temperatures, the predominant reaction mode of the jet in water was stable film boiling, and the metal droplets fell in liquid form without steam explosions.

In Section 3.1, when the water temperature was set at 25°C and the jet temperature was 1100°C, steam explosions occurred in all experiments. Partial experiments with a jet temperature of 1200°C also observed steam explosions, while no steam explosions were observed in experiments at 1300°C. When the water temperature was at room temperature, as the temperature of the molten metal decreases, the relationship between the water and the molten metal becomes more akin to the Thermal Interaction Zone, leading to a higher probability of steam explosions (as shown in Fig. 2). Under this condition, the melt temperature directly influenced the occurrence of steam explosions.
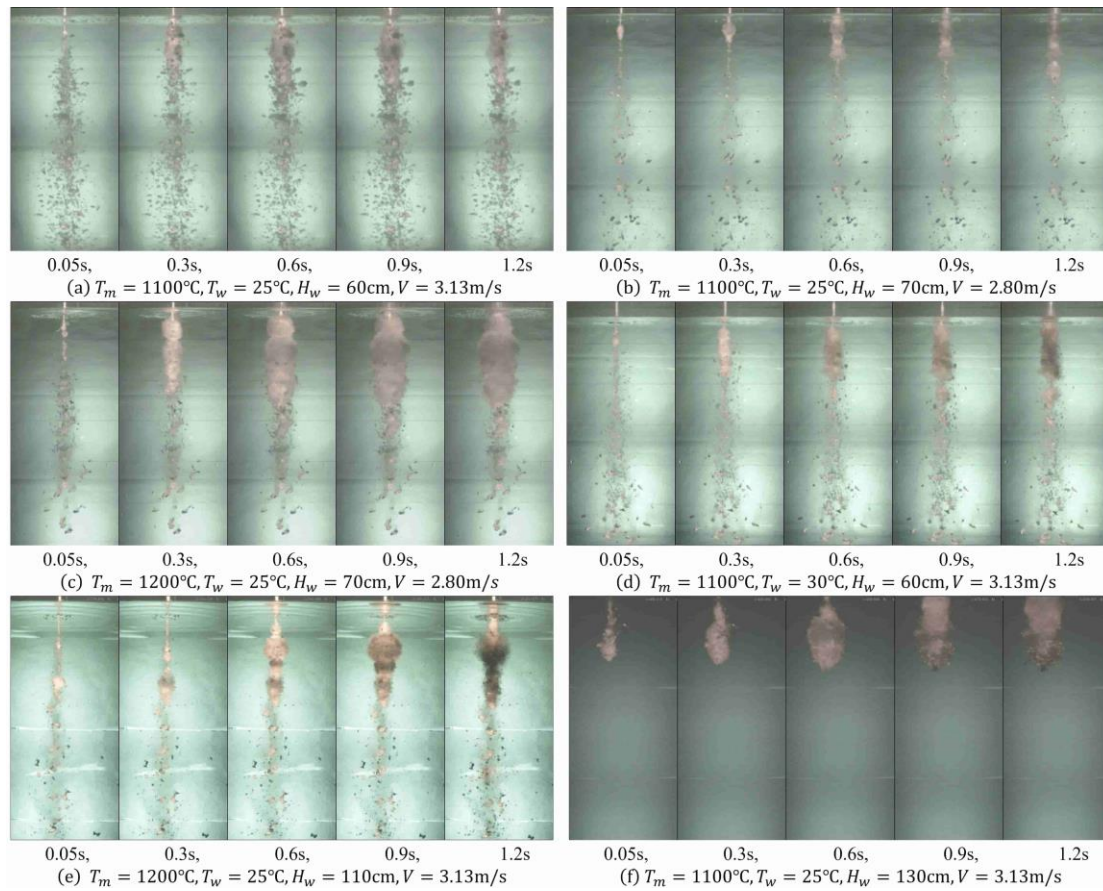

0.05s, 0.3s, 0.6s, 0.9s, 1.2s
(a) $T_m = 1100°C, T_w = 25°C, H_w = 60cm, V = 3.13m/s$

0.05s, 0.3s, 0.6s, 0.9s, 1.2s
(b) $T_m = 1100°C, T_w = 25°C, H_w = 70cm, V = 2.80m/s$

0.05s, 0.3s, 0.6s, 0.9s, 1.2s
(c) $T_m = 1200°C, T_w = 25°C, H_w = 70cm, V = 2.80m/s$

0.05s, 0.3s, 0.6s, 0.9s, 1.2s
(d) $T_m = 1100°C, T_w = 30°C, H_w = 60cm, V = 3.13m/s$

0.05s, 0.3s, 0.6s, 0.9s, 1.2s
(e) $T_m = 1200°C, T_w = 25°C, H_w = 110cm, V = 3.13m/s$

0.05s, 0.3s, 0.6s, 0.9s, 1.2s
(f) $T_m = 1100°C, T_w = 25°C, H_w = 130cm, V = 3.13m/s$

Fig. 18. Samples of the steam explosions

3.6. Comparison between experimental results and fragmentation theories

When the molten copper jet enters the cooling water, the interface between the molten copper jet and the cooling water is subject to fluctuations due to the instability of external oscillation waves. The growth of the wavelength easily leads to the rupture of the vapor film, exacerbating the fragmentation behavior of the molten copper. These external oscillation waves mainly include Kelvin-Helmholtz instability (K-H instability), Rayleigh-Taylor instability (R-T instability).

Kelvin-Helmholtz (K-H) instability refers to the instability phenomenon that occurs at the interface between two different fluids with a velocity difference or within a continuous fluid with shear velocity. The most-unstable wavelength of K-H instability λ_{K-H} is given by the following equation (Iwasawa and Abe, 2019):

$$\lambda_{K\text{-}H} = \frac{2\pi\sigma_m(\rho_m + \rho_c)}{u^2\rho_m\rho_c} \tag{8}$$

where ρ_m represents the density of the molten metal (kg/m³), ρ_c is the density of the coolant (kg/m³), σ_m is the surface tension of the molten metal (N/m), u represents the relative velocity between the two fluids at the interface, which in this case is the penetration velocity V of the molten metal.

The Rayleigh-Taylor (R-T) instability, which originates due to the disparity in inertia forces between two fluids at the surface wave, predominantly takes place at the foremost part of the melt jet when it vertically intrudes into the interface during melt - coolant interactions. The wavelength related to the most rapid growth rate of R-T instability can be represented by the following equation (Iwasawa and Abe, 2019):

$$\lambda_{R\text{-}T} = 2\pi\sqrt{\frac{\sigma_m}{(\rho_m - \rho_c)g}} \tag{9}$$

On the contact surface between the molten material and the coolant, the shear force from the relative velocity of the fluids balances the surface tension on the molten metal

droplets. The disruption occurs when this equilibrium is broken. To predict the occurrence of disruption, the Weber number (We) is an important dimensionless parameter, defined as(Iwasawa and Abe, 2019):

$$We = \frac{\rho_c V^2 d}{\sigma_m} \tag{10}$$

where We is the Weber number; V stands for the velocity (m/s) at which the molten metal makes contact with the coolant, which is the melt penetration velocity in this experiment. σ_m denotes the surface tension (N/m) of the molten metal, and d is the diameter (mm) of the molten metal droplet.

Saito et al. proposed the following Weber number calculation method based on the mass mean diameter of fragments (Saito et al., 2016):

$$We = C Re_w^{\frac{2}{3}} \left(\frac{\rho_w}{\rho_m}\right)^{-\frac{1}{3}} \left(\frac{\mu_w}{\mu_m}\right)^{\frac{2}{3}} \tag{11}$$

where C is an empirical coefficient. μ_w represents the dynamic viscosity of water, while μ_m represents the dynamic viscosity of the molten material jet. Re_w represents the Reynolds number of water at the characteristic length D and is calculated using the following formula:

$$Re_w = \frac{\rho_w V D}{\mu_w} \tag{12}$$

where V is the penetration velocity of the molten material jet, and D can be viewed as the diameter of the molten metal droplet d in this context. The diameter of the molten metal droplet is assumed to be equal to the mass mean diameter of the fragments. After fitting, coefficient C was taken as 0.02. By combining Eqs. (10), (11) and (12), d can be expressed as a function of V as follows:

$$d = 8 \times 10^{-6} \frac{\rho_m \sigma_m{}^3}{(\rho_w \mu_m)^2 V^4} \tag{13}$$

Fig. 19 offers a comparison of experimental results with R-T instability, K-H instability, and Weber number theories. The graph shows that, in contrast to other fragmentation theories, the Weber number theory is better at predicting the mass mean diameter of the fragments. This may be because the Weber number takes into account the interaction

between the surface tension of the molten jet and the shear force of the water.
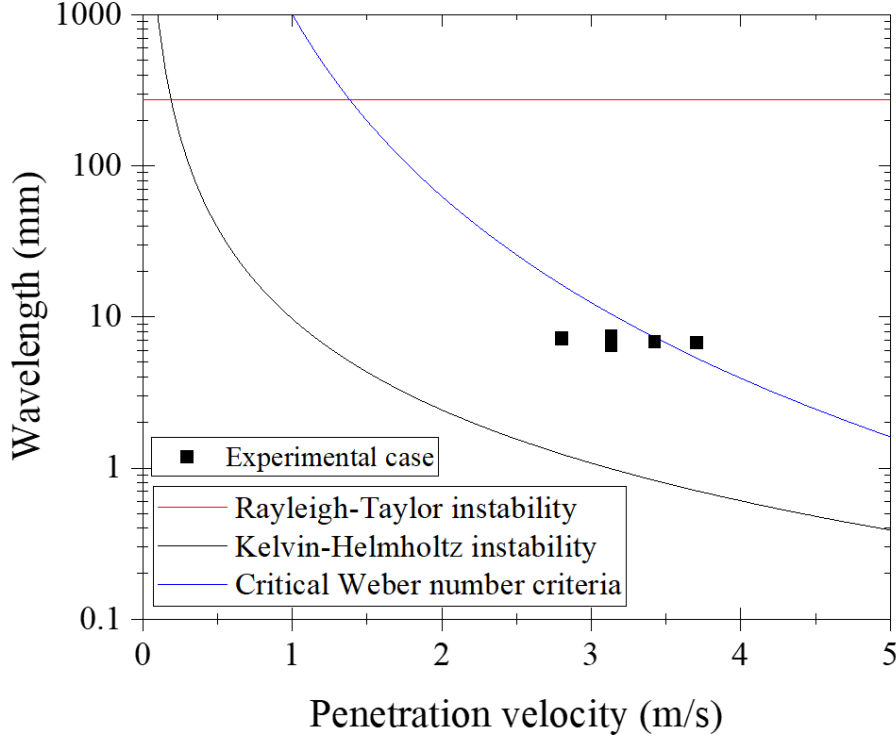

Fig. 19. Most unstable wavelength for Kelvin-Helmholtz instability, Rayleigh-Taylor instability and

Weber number theory

4. Conclusions

In order to gain a deeper understanding of the molten fuel fragmentation behavior, a set of simulated experiments were carried out. These experiments involved introducing molten copper into water with varying melt temperatures, water temperatures, penetration velocities, and water depths. Our extensive discussions covered the impact of these parameters on the jet fragmentation processes, the morphology of the debris bed, the form of fragmentation products, the size distribution of fragments, the mass mean diameter of fragments, the porosity of the fragment bed, and the sphericity of fragment particles. By comparing the experimental results with theoretical predictions,

the following conclusions were drawn:

(1) As molten material temperatures rise, fragmentation products become larger, resulting in a denser fragment bed and more spherical particles.

(2) As water temperatures go up, the vapor film between the molten copper jet and water stabilizes, causing large agglomerates to form at the bottom.

(3) Greater melt penetration velocity intensifies the fragmentation effect, producing smaller fragments. However, it doesn't significantly affect debris bed porosity or fragment sphericity.

(4) Except when large aggregates form at shallow water depths and high copper superheat, water depth has little impact on the melt jet's fragmentation behavior.

(5) The Weber number theory outperforms Rayleigh-Taylor and Kelvin-Helmholtz instability theories in predicting the mass mean diameter of debris.

References

Abe, Y., Kizu, T., Arai, T., Nariai, H., Chitose, K., Koyama, K., 2004. Study on thermal-hydraulic behavior during molten material and coolant interaction. Nucl. Eng. Des. 230, 277–291. https://doi.org/10.1016/j.nucengdes.2003.11.032

Abe, Y., Matsuo, E., Arai, T., Nariai, H., Chitose, K., Koyama, K., Itoh, K., 2006. Fragmentation behavior during molten material and coolant interactions. Nucl. Eng. Des. 236, 1668–1681. https://doi.org/10.1016/j.nucengdes.2006.04.008

Bürger, M., Cho, S.H., Berg, E. v., Schatz, A., 1995. Breakup of melt jets as pre-condition for premixing: Modeling and experimental verification. Nucl. Eng. Des. 155, 215–251. https://doi.org/10.1016/0029-5493(94)00875-Y

Cheng, H., Chen, X., Ye, Y., Cheng, S., 2021. Systematic experimental investigation on the characteristics of molten lead-bismuth eutectic fragmentation in water. Nucl. Eng. Des. 371, 110943. https://doi.org/10.1016/j.nucengdes.2020.110943

Cheng, H., Cheng, S., Zhao, J., 2020. Study on corium jet breakup and fragmentation in sodium with a GPU-accelerated color-gradient lattice Boltzmann solver. Int. J. Multiph. Flow 126, 103264. https://doi.org/10.1016/j.ijmultiphaseflow.2020.103264

Cheng, H., Tan, S., Cheng, S., 2022. Study on the effect of jet cross section shape on molten fuel fragmentation behavior with simulant experiments. Nucl. Eng. Des. 400, 112077. https://doi.org/10.1016/j.nucengdes.2022.112077

Cheng, S., Gong, P., Wang, S., Cui, J., Qian, Y., Zhang, T., Jiang, G., 2018. Investigation of flow regime in debris bed formation behavior with nonspherical particles. Nucl. Eng. Technol. 50, 43–53. https://doi.org/10.1016/j.net.2017.09.003

Dinh, T.N., Bui, V.A., Nourgaliev, R.R., Green, J.A., Sehgal, B.R., 1999. Experimental and analytical studies of melt jet-coolant interactions: a synthesis. Nucl. Eng. Des. 189, 299–327. https://doi.org/10.1016/S0029-5493(98)00275-1

ERGUN, S., 1952. Fluid Flow Through Packed Columns. Chem. Eng. Prog. 48, 89.

Gabor, J.D., Purviance, R.T., Aeschlimann, R.W., Spencer, B.W., 1988. Breakup and quench of molten metal fuel in sodium (No. CONF-880506-20). Argonne National Lab., IL (USA).

Hu, L., Ge, K., Zhang, Y., Su, G.H., Tian, W., Qiu, S., 2019. Fragmentation characteristics of molten materials jet dropped into liquid sodium pool. Nucl. Eng. Des. 355, 110348. https://doi.org/10.1016/j.nucengdes.2019.110348

Hu, L., Ge, K., Zhang, Y., Zhang, D., Su, G.H., Tian, W., Qiu, S., 2020. Experimental research on fragmentation characteristics of molten stainless steel discharged into sodium pool and comparison with molten copper. Prog. Nucl. Energy 118, 103069. https://doi.org/10.1016/j.pnucene.2019.103069

Huhtiniemi, I., Magallon, D., Hohmann, H., 1999. Results of recent KROTOS FCI tests: alumina versus corium melts. Nucl. Eng. Des. 189, 379–389. https://doi.org/10.1016/S0029-5493(98)00269-6

Iwasawa, Y., Abe, Y., 2019. Scaling analysis of melt jets and solidification modes. Ann. Nucl. Energy 125, 231–241. https://doi.org/10.1016/j.anucene.2018.10.059

Iwasawa, Y., Abe, Y., 2018. Melt jet-breakup and fragmentation phenomena in nuclear reactors: A review of experimental works and solidification effects. Prog. Nucl. Energy 108, 188–203. https://doi.org/10.1016/j.pnucene.2018.05.009

Kondo, Sa., Konishi, K., Isozaki, M., Imahori, S., Furutani, A., Brear, D.J., 1995. Experimental study on simulated molten jet-coolant interactions. Nucl. Eng. Des. 155,

73–84. https://doi.org/10.1016/0029-5493(94)00870-5

Leskovar, M., Uršič, M., 2009. Estimation of ex-vessel steam explosion pressure loads. Nucl. Eng. Des. 239, 2444–2458. https://doi.org/10.1016/j.nucengdes.2009.07.023

Magallon, D., Huhtiniemi, I., Hohmann, H., 1999. Lessons learnt from FARO/TERMOS corium melt quenching experiments. Nucl. Eng. Des. 189, 223–238. https://doi.org/10.1016/S0029-5493(98)00274-X

Saito, R., Abe, Y., Yoshida, H., 2016. Breakup and fragmentation behavior of molten material jet in multi-channel of BWR lower plenum. J. Nucl. Sci. Technol. 53, 147–160. https://doi.org/10.1080/00223131.2015.1027756

Shen, P., Zhou, W., Cassiaut-Louis, N., Journeau, C., Piluso, P., Liao, Y., 2018. Corium behavior and steam explosion risks: A review of experiments. Ann. Nucl. Energy 121, 162–176. https://doi.org/10.1016/j.anucene.2018.07.029

Spencer, B.W., Wang, K., Blomquist, C.A., McUmber, L.M., Schneider, J.P., 1994. Fragmentation and quench behavior of corium melt streams in water (No. NUREG/CR-6133; ANL-93/32). Nuclear Regulatory Commission, Washington, DC (United States). Div. of Systems Research; Argonne National Lab. (ANL), Argonne, IL (United States). https://doi.org/10.2172/10136350

Yang, Z., Zhang, Z.-G., Liu, C., Ji, B., Ahmed, R., 2019. Thermal and hydrodynamic fragmentation of continuous molten copper droplets penetrating into sodium pool. Int. Commun. Heat Mass Transf. 108, 104317. https://doi.org/10.1016/j.icheatmasstransfer.2019.104317